

Effects of bed roughness on boundary layer mixing and mass flux across the sediment-water interface

M. A. Reidenbach,¹ M. Limm,² M. Hondzo,³ and M. T. Stacey⁴

Received 26 May 2009; revised 11 March 2010; accepted 22 March 2010; published 23 July 2010.

[1] Fine-scale measurements of boundary layer flow and solute transport were conducted within a laboratory flume to determine how bed topography influences mixing and mass transport at the sediment-water interface. Three different bed topographies were examined, with roughness composed of sand, gravel, or cobbles. Fluorescein dye, used as a dissolved tracer, was injected into the flow, and concentration and velocity were simultaneously measured using a combined planar laser-induced fluorescence and particle image velocimetry technique. Enhanced turbulent mixing due to bed roughness increased mass flux across the sediment-water interface between 1.3 times greater for the sand and 7.5 times greater for the cobble bed compared to estimates over a hydraulically smooth surface. As bed roughness increased, mass exchange became spatially more heterogeneous, coinciding with a transition from a boundary layer to a shear-dominated mixing layer in the near-wake region behind individual roughness elements. The enhanced flux increased pore water concentrations. However, for the same bed geometry, increased mean flow within the water column locally reduced pore water concentrations, likely due to greater downstream transport and dispersion occurring within the bed.

Citation: Reidenbach, M. A., M. Limm, M. Hondzo, and M. T. Stacey (2010), Effects of bed roughness on boundary layer mixing and mass flux across the sediment-water interface, *Water Resour. Res.*, 46, W07530, doi:10.1029/2009WR008248.

1. Introduction

[2] The transport of water and material through a river control the particle size distribution of bed sediments at a given point in a watershed. Alterations to this transport by humans and/or natural causes can lead to a coarsening or fining of the bed, altering the bed topography. The interaction between the bottom topography formed by these sediments and the overlying boundary layer flow can drive exchange of both dissolved and particulate matter between pore waters and the water column [Hondzo, 1998; Huettel *et al.*, 1996]. This can alter chemical retention within the bed sediments, impact surface water quality [Ryan *et al.*, 2007], and modify local benthic algal production and biogeochemical processes occurring adjacent to the sediment surface [Battin *et al.*, 2003; Finlay *et al.*, 1999]. Knowledge of the mean flow and turbulence structure associated with various streambed topographies is essential to understanding chemical exchange at the sediment-water interface as well as momentum and energy fluxes between the water column and the bed [Dawson and Trass, 1972; Kader and Yaglom, 1972].

[3] Of interest in this study are processes occurring within the water column that drive solute exchange to and from streambed sediments. Processes in the hyporheic zone are governed by flow dynamics within the turbulent bottom boundary layer (BBL), diffusion across the diffusive sublayer (DSL), and transport through the permeable bed sediments [Packman *et al.*, 2004]. The vertical transport within the BBL is typically dominated by turbulent eddy diffusion, which depends upon the rates of mixing and the dissipation rate of turbulent kinetic energy in the mean flow [Lorke *et al.*, 2003]. A region typically exists within the BBL, where the flow profile is logarithmic and can be described by the equation [Kundu, 1990; Nikora *et al.*, 2001],

$$U(z) = \frac{u_*}{\kappa} \ln\left(\frac{z - d_o}{z_o}\right), \quad (1)$$

where u_* is the friction velocity, κ is von Karman's constant ($= 0.41$), z_o is the roughness length scale, and d_o is the origin displacement for the bed location [Stacey *et al.*, 1999]. For flows above roughness elements, d_o is essentially the zero-plane displacement, which corresponds to the mean level of momentum absorption [Nepf and Vivoni, 2000]. The friction velocity is directly related to the amount of turbulence and momentum transfer occurring within the boundary layer.

[4] Below the logarithmic region and close to the bed is the diffusive sublayer, where the magnitude of the turbulent eddy diffusivity decreases and the vertical transport of mass is dominated by molecular diffusion. Viscous forces limit turbulent motions within the DSL, and the velocity profile within this layer is linear with respect to height. Although the DSL is very thin relative to the size of the overall

¹Department of Environmental Sciences, University of Virginia, Charlottesville, Virginia, USA.

²Department of Integrative Biology, University of California, Berkeley, California, USA.

³St. Anthony Falls Laboratory, Department of Civil Engineering, University of Minnesota, Minneapolis, Minnesota, USA.

⁴Department of Civil and Environmental Engineering, University of California, Berkeley, California, USA.

boundary layer, it plays a key role in controlling transport across the sediment-water interface. Reducing the thickness of the DSL or periodically disrupting its formation through sweep-ejection events of overturning eddies [O'Connor and Hondzo, 2008] can greatly enhance the transfer of dissolved substances to and from sediment pore waters [Roy et al., 2002]. Diffusive flux across the sediment-water interface is often calculated using Fick's law of diffusion,

$$\text{Flux} = -D \left. \frac{d\bar{c}}{dz} \right|_{z=0}, \quad (2)$$

where D is the molecular diffusivity, \bar{c} is the mean concentration, and $d\bar{c}/dz$ is the time-averaged vertical concentration gradient. Equation (2) assumes that the sediment-water interface is an infinite flat plane, with a uniform one-dimensional concentration gradient. Since the diffusive sublayer is very thin, it is often difficult to measure the concentration gradient in this layer, and equation (2) is simplified by defining a mass transfer coefficient β ,

$$\text{Flux} = -\beta(c_\infty - c_0), \quad (3)$$

where c_0 is the concentration at the interface and c_∞ is the concentration in the overlying flow. Within the DSL, the time-averaged vertical concentration gradient should be constant [Lorke et al., 2003], and $\beta = D/\delta$, where δ is the thickness of the diffusive sublayer. A variety of empirical formulas have been formed for β that relate flow processes and bed shear characteristics to mass transfer over smooth beds, which typically take the form [Berger et al., 1979; Kader and Yaglom, 1972; Shaw and Hanratty, 1977],

$$\beta = c_2 u_* Sc^n, \quad (4)$$

where c_2 and n are empirically derived coefficients, u_* is the shear velocity, and $Sc = \nu/D$ is the Schmidt number. For example, Hondzo [1998] obtained a relationship for O_2 flux through the diffusive sublayer with values for the coefficients $c_2 = 0.0588$ and $n = -2/3$. Slight variations have been found for the coefficients [reviewed in Boudreau and Jorgensen, 2001], yet their predictions for β over a uniform flat bed are quite similar.

[5] In natural systems, both small-scale O (micrometer to millimeter) and larger-scale O (centimeter to meter) roughness are common and act to periodically disrupt the diffusive sublayer to create spatial and temporal variations in concentration gradients near the sediment-water interface. As topographic variability and roughness length scales increase, bed roughness can further disrupt the boundary layer flow structure, creating a transition from rough boundary layer conditions to the formation of turbulent shear layers in the near-wake region behind individual roughness elements. Formation of shear layers show marked differences from typical boundary layers, including turbulence structure, the behavior of the turbulent kinetic energy balance, and efficiency of momentum transfer [Lacey and Roy, 2008]. The shear layer is also characterized by an inflection in the mean velocity profile, in contrast with the boundary layer flow. This inflection induces instabilities which form coherent eddies within the fully-developed turbulent flow. Turbulent motions transfer momentum through the boundary layer, mix solutes within the water column, and transport these

solutes to and from the sediment-water interface. Solute flux can be very intermittent both in space and time, and as the bed topography becomes spatially more variable, the assumptions used to apply Fick's law become less valid.

[6] Measurements of mass transport are often accomplished using chamber measurements, which measure bulk biologically controlled transport rates [i.e., Glud et al., 1998] or through microelectrodes [i.e., Roy et al., 2002; Steinberger and Hondzo, 1999], which can determine the fine-scale structure of the DSL across the sediment-water interface. Due to topographic variability, hydrodynamics often control rates of exchange, and local measurements may not be indicative of overall flux. Bed roughness enhances turbulence within the boundary layer flow and well-defined turbulence ejection events, which transfer low-momentum fluid from near the bed and sweep events which transfer high-momentum fluid toward the bed, often occur [Grass, 1971]. These flow interactions can also transfer momentum between the overlying and subsurface flow [Packman and Salehin, 2003], influencing the thickness and location of the DSL and creating both horizontal and vertical gradients in flux along the bed [Roy et al., 2002]. Over topography that creates high variability in DSL dynamics, such as highly permeable sands, it is often more advantageous to measure the vertical transport of solutes to the bed from direct measurements of turbulent flow and mixing process occurring above the bed [Berg et al., 2007]. Since mass flux is a volumetric rate of transport, direct estimates of mass flux across the sediment-water interface can be quantified if simultaneous measures of solute concentration and velocity can be made. A mathematical expression for the vertical flux at any point in space or time due to advection and molecular diffusion is [Berg et al., 2003],

$$\text{Flux} = wc - D \frac{\partial c}{\partial z}, \quad (5)$$

where w and c are the instantaneous vertical velocity and solute concentration, respectively. Typically, velocity and concentration are separated into time-averaged and turbulent fluctuations, $w = \bar{w} + w'$ and $c = \bar{c} + c'$. The separation can then be substituted into equation (5) and averaged over a time period significantly longer than the time scale of turbulent fluctuations. It is typically assumed that $\bar{w} \sim 0$ adjacent to the bed and the time averaged flux can then be determined as

$$\overline{\text{Flux}} = \overline{w'c'} - D \frac{\partial \bar{c}}{\partial z}. \quad (6)$$

Mean flux to the sediment-water interface is thus the sum of the turbulent ($\overline{w'c'}$) and diffusive ($-D\partial\bar{c}/\partial z$) mechanisms. Most estimates of flux using direct measures within the diffusive boundary layer have focused on the diffusive term, since only high-energy eddies will typically penetrate the region of the DSL. However, for energetic flows or flows over rough beds, turbulent fluctuations become more important and typically dominate outside the viscous sublayer of flow [Boudreau and Jorgensen, 2001].

[7] The goal of this study is to determine the effect of bed roughness on water column turbulence and the vertical flux of solutes within the bottom boundary layer. Of particular interest are how bed roughness alters the magnitude and

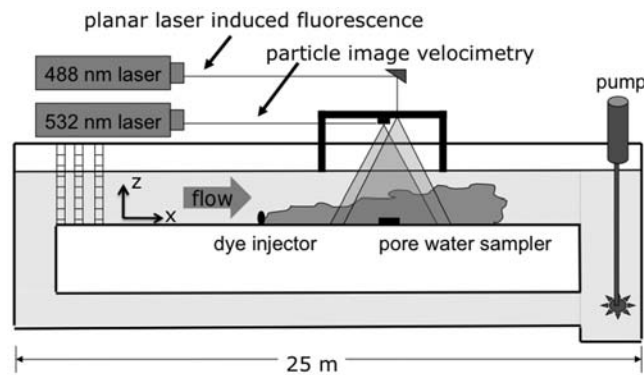


Figure 1. Schematic of recirculating flume. Two laser systems were used, a 488 nm laser to conduct planar laser-induced fluorescence and a 532 nm laser for particle image velocimetry. Pore water concentrations 0.5 cm below the sediment surface were monitored using a gravity feed to a Turner Designs© 10 AU fluorometer.

structure of turbulence within the bottom boundary layer and how these hydrodynamic processes affect mass flux to the sediment-water interface. In these highly dynamic regions near benthic roughness, both the turbulent and diffusive component of the flux may be nonnegligible and need to be measured concurrently. To measure total mass flux, simultaneous measurements of velocity and scalar concentrations must be made at the same location within the water column. A combined planar laser-induced fluorescence (PLIF) and particle image velocimetry (PIV) technique was developed to measure scalar concentrations and velocity at an imaging rate of 50 Hz over an 8 cm × 8 cm sampling window. Three different bed roughness conditions were tested, which ranged from a smooth sand bed ($d_{50} = 1.5$ mm) to that of a gravel bed ($d_{50} = 6.5$ mm), and at the largest roughness, one whose topography consisted of medium sized cobbles (mean diameter of 100 mm and height of 30 mm).

2. Materials and Methods

2.1. Flume and Sediment

[8] The experimental work was conducted in a recirculating laboratory flume with dimensions of 25 m long, 0.6 m wide, and 0.3 m high. The flume was set to a surface slope of 0° and unidirectional flow was created by a variable drive impeller pump, located at the downstream end of the tank (Figure 1). The walls of the tank are made of optically clear glass, while the base of the flume is flat sheet metal. The flume was filled with freshwater, and water depth was controlled for all experiments at $H = 0.25$ m relative to the elevation of the bed. To condition the turbulence and minimize secondary circulation, three sets of grids containing 1 cm wide square openings were placed at the upstream end of the flume. Five meters downstream from the leading edge of the flume, a 12 m long section of bed material, composed of either sand (labeled as S in Table 1), sand with an overlying layer of gravel (G), or sand/gravel with an overlying layer of cobbles (C), was placed on the flume floor (Figure 2). Cobbles were added randomly to the flume, with a mean relative spacing between cobbles of approximately 30 cm.

Due to the nonuniform spacing of the cobbles, the 25 cm water depth was measured relative to the base of the cobbles, at the elevation of the underlying gravel bed material. To ensure a well-developed boundary layer, measurements of velocity and solute concentration were made 13 m downstream from the leading edge of the flume and 8 m downstream from the leading edge of the bed material. Scaling arguments suggest that the thickness δ of a turbulent boundary layer grows as fluid moves over a flat plate as [Schlichting and Gersten, 2000]

$$\delta = 0.37L \left(\frac{UL}{\nu} \right)^{-0.2}, \quad (7)$$

where U is the mean velocity, ν is the kinematic viscosity of water, and L is the downstream distance from the leading edge of the flat plate. For velocity conditions tested, the boundary layer at $L = 13$ m would be fully developed throughout the water column if no sediment was added to the flume. However, for our experimental setup, there is a transition from a smooth to rough bed surface, essentially causing the growth of an internal boundary layer over the bed material. Boundary layer growth response to a roughness change has been studied by *Antonia and Luxton* [1971], who found that the readjustment of the boundary layer from a smooth to rough bed condition takes place at a distance of approximately 20 boundary layer thicknesses from the start of the roughness. Therefore, the distance at which the boundary layer would be fully developed throughout the water depth is 5.0 m downstream from the addition of the bed material. In total, nine experiments were carried out in the laboratory flume using three different velocities tested over the three different types of bed material. Experiments are listed, along with boundary layer characteristics, in Table 1.

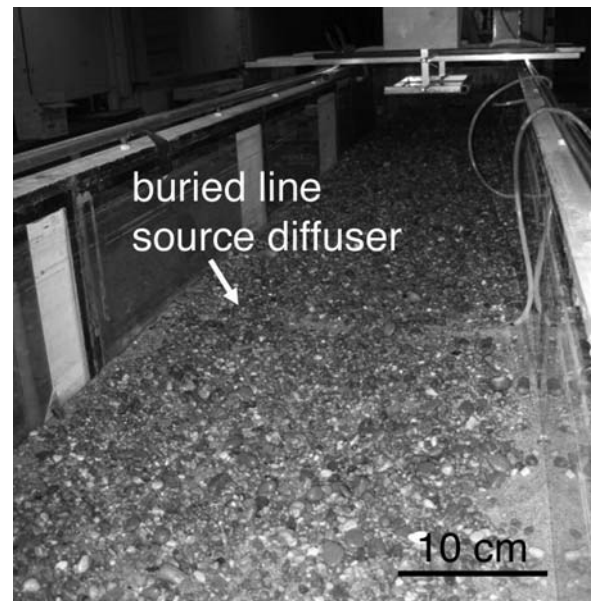


Figure 2. Along-channel image of the flume test section containing the gravel bed (G). Location of the line source diffuser is indicated. PLIF/PIV imaging was conducted 1 m downstream of the line source.

Table 1. Flow and Turbulence Characteristics for the Sand, Gravel, and Cobble Bed Geometry Experiments^a

| Experiment | U_o (cm s ⁻¹) | u_{*rs} (cm s ⁻¹) | u_* (cm s ⁻¹) | z_o (cm) | Re_* | ϵ (cm ² s ⁻³) | Kolmogorov length (mm) |
|------------|-----------------------------|---------------------------------|-----------------------------|------------|--------|-----------------------------------------------|------------------------|
| S1 | 6.8 | 0.37 | 0.36 | 0.003 | 5.4 | 0.03 | 0.76 |
| S2 | 8.9 | 0.48 | 0.47 | 0.004 | 7.0 | 0.08 | 0.59 |
| S3 | 11.2 | 0.52 | 0.62 | 0.007 | 9.3 | 0.17 | 0.49 |
| G1 | 5.9 | 0.49 | 0.55 | 0.086 | 35.8 | 0.14 | 0.52 |
| G2 | 7.1 | 0.57 | 0.66 | 0.091 | 42.9 | 0.22 | 0.46 |
| G3 | 9.0 | 0.66 | 0.79 | 0.083 | 51.3 | 0.44 | 0.39 |
| C1 | 5.5 | 0.62 | 0.80 | 0.482 | 240 | 0.32 | 0.42 |
| C2 | 6.8 | 0.87 | 0.95 | 0.439 | 285 | 0.52 | 0.37 |
| C3 | 8.0 | 1.12 | 0.96 | 0.338 | 288 | 0.63 | 0.35 |

^aMean velocity U_o (cm s⁻¹) was measured at 6 cm above the bed. u_{*rs} is the friction velocity computed from equation (8) using Reynolds stress estimates, while u_* and the roughness length scale z_o were computed from equation (1). The roughness Reynolds number was computed as $Re_* = u_* d_g/\nu$, and ϵ is the dissipation rate of TKE, measured at $z/H = 0.1$. S, sand; G, gravel; C, cobble bed.

[9] Disodium fluorescein dye (molecular diffusivity, $D = 5.1 \times 10^{-6}$ cm² s⁻¹) with a source concentration C_{source} between 50 and 100 $\mu\text{g cm}^{-3}$ was used as the tracer. Fluorescein has a $Sc = 1970$ at 20°C. Dye was injected uniformly across the width of the flume using a line source diffuser. The diffuser was constructed of 1 cm diameter Tygon® tubing with 2 mm diameter holes punched along the tubing in 2 cm increments to release the dye. The diffuser, which ran across the flume width, was attached to a Plexiglas plate and buried in the sediment so that dye release was adjacent to the bed surface. Dye was supplied at a rate of 0.04 L/min from a 4 L constant head container positioned over the flume. After each set of experiments, the flume was drained and flushed to remove any residual dye and refilled before further experiments were conducted with a different bed geometry.

2.2. Combined Planar Laser-Induced Fluorescences and Particle Image Velocimetry

[10] Fluorescein concentrations and velocity structure were simultaneously measured over an 8 cm \times 8 cm area using combined measurements of planar laser-induced fluorescence (PLIF) and particle image velocimetry (PIV). The PLIF system consisted of a laser, optics to expand and focus the laser light, a scanning mirror to produce a sheet of light, and a digital CCD camera to record the dye fluorescence in the flowing water. Laser light with a mixed wavelength between 488 and 514 nm (blue-green light) was emitted by an argon ion laser (American 60 \times) at an output intensity of 100 mW. The laser beam was first expanded and then focused using a 3 \times laser expander (Melles Griot®). A light sheet was created using a moving magnet optical scanning mirror (Cambridge Technology model 6800HP). The light sheet first passed through a glass window insert that was suspended over the flume and contacted the water surface in order to minimize laser diffraction by small ripples on the water surface. This sheet illuminated a 0.2 cm thick \times 10 cm wide vertical slice through the water column parallel to the main flow direction. Dye was released 1 m upstream (nondimensional downstream distance of $x/H = 4$) of the imaging area. As the dye passed through the laser light sheet, the fluoresced dye was imaged using a digital camera (Redlake Motionscope PCI with 480 \times 420 pixel resolution) with a 25 mm, $f/0.95$ fixed lens (Navitar, Inc.). The camera was fitted with a 525 nm optical long-pass filter (Andover Corp.), which blocked ambient laser light but allowed emitted light from the fluoresced dye to be imaged

(Figure 3). The laser sheet was scanned to illuminate the imaging field every 0.02 s, with a wait period of 0.02 s between each scan.

[11] A second laser with an output wavelength of light at 532 nm was used for PIV imaging. Silver-coated hollow glass spheres (11 μm in diameter, Potter Industries) were added to the flume water and well mixed prior to the start of the experiments. The PIV laser was pulsed at 0.02 s intervals at alternating time periods when the PLIF laser was not being scanned. The pulsed laser was passed through a 30° cylindrical lens to create a light sheet 0.2 cm thick and 10 cm wide, aligned along the same two-dimensional plane as the PLIF laser. During the experiments, particles were passively carried in the flowing water and illuminated in the imaging area with the PIV laser. Using the same Redlake motion-scope camera as in the PLIF imaging, reflected light from the particles were illuminated at 532 nm. Since 532 nm is outside the absorption band of fluorescein, the PIV laser did not excite the fluorescein dye. Therefore, during the PLIF laser scan, only fluoresced dye was imaged, while during the PIV laser pulse, only particles were imaged. The image capture rate was 50 frames per second, and 10,000 total images were obtained for each flow condition, containing 5000 PIV images and 5000 PLIF images.

[12] PIV images were processed using MatPIV 1.6.1 software written for Matlab® [Sveen, 2004] using a hybrid digital PIV technique [Cowen and Monismith, 1997]. This software divides each frame of each run into an array of “interrogation subwindows” and calculates the most probable displacements of particles in successive pairs of frames using cross-correlation analysis. The final output from the software produces a horizontal and vertical velocity estimate for every 8 \times 8 pixel subwindow, giving 59 \times 51 velocity measurements per image pair. This corresponds to a velocity estimate every 0.13 cm in both the vertical and horizontal dimensions. Accuracy of the PIV measurements was estimated using a separate calibration facility where the camera was towed across a flume at a known speed (facility described in the work of Reidenbach *et al.* [2008]). For the framing rate used, the accuracy of the velocity measurements was found to be relative to the mean velocity of the flow U , with an overall accuracy of $\pm 6\% U$.

[13] For the PLIF images, a dye source concentration of 50–100 $\mu\text{g cm}^{-3}$ was chosen so that at the imaging location, peak concentrations were approximately 5–10 $\mu\text{g cm}^{-3}$. This concentration maximized the full dynamic range of the camera but minimized errors due to photo bleaching or

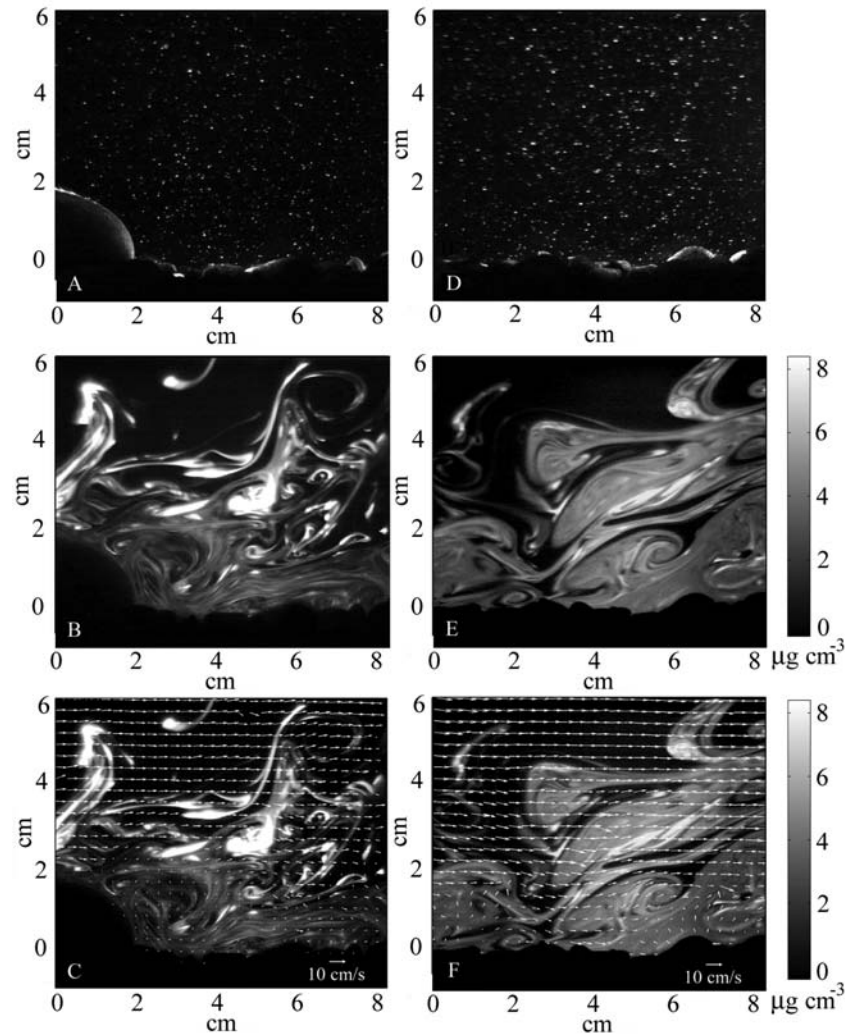


Figure 3. (a) Particle image velocimetry image of flow over the cobble bed, (b) planar laser-induced fluorescence image of fluorescein dye taken 0.02 s after the PIV image, and (c) combined PLIF image with velocity vectors computed using cross-correlation analysis of particle motion between images taken 0.02 s before and 0.02 s after the PLIF image. (d–f) Similar images obtained over the gravel bed.

absorption issues [Ferrier *et al.*, 1993]. An in situ calibration was performed to convert pixel intensity to concentration.

2.3. Pore Water Sampling

[14] To sample the concentration of dye in the sediment pore water, a 10 cm × 10 cm Plexiglas plate was buried 0.5 cm below the sediment surface directly below the imaging area. The plate was 0.3 cm thick to minimize the impact on the downstream transport of fluid and dye within the sediment pore waters. A 1.5 cm diameter hole was cut in the Plexiglas and a Tygon tube was attached to the hole and filled with a porous sponge to prevent clogging by the sediments. Water was siphoned by gravity feed directly to a Turner Design 10 AU fluorometer that continuously monitored pore water concentrations at a rate of 1 Hz using a flow-through system. The flow through the tube was adjusted by a control valve and limited in an attempt to minimize the impact that the siphoning had on water column flow and turbulence processes. At the beginning of every experiment and at 1 min intervals during the experiments, a

20 mL sample of water was taken upstream of the test section to monitor changes in background concentrations of dye in the flume. These background concentrations were subtracted from pore water sample levels to remove bias in the measurements due to increases in background dye levels. Mean pore water concentrations were computed over a 10 min sampling period while PLIF/PIV imaging was being conducted.

2.4. Data Analysis

[15] PIV measurements of horizontal and vertical velocities were obtained by averaging particle motions within each 8 × 8 pixel subwindow. Image pairs yielded 3000 velocity vectors spaced evenly every 0.13 cm across the imaging field. Concentrations were computed at each pixel, which had a square dimension of 0.017 cm × 0.017 cm. To calculate turbulent flux ($w'c'$), mean and fluctuating scalar concentrations were averaged to the same 8 × 8 pixel subwindow computed for velocity. The mean and fluctuating part of the longitudinal velocity were computed as $u = \bar{u} + u'$,

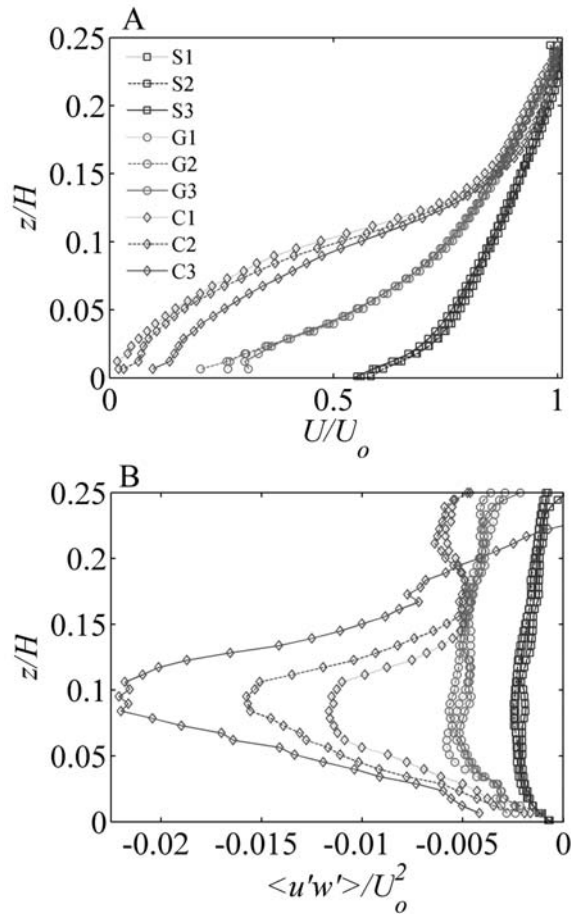


Figure 4. Horizontally averaged (a) velocity and (b) turbulent Reynolds stress ($\overline{u'w'}$). U is the mean velocity, and U_o is the reference velocity measured at $z/H = 0.25$. Note the strong shear layer formed due to flow over a cobble (C1, C2, and C3), whose height was approximately $z/H = 0.1$ above the bed.

along with vertical velocity $w = \bar{w} + w'$ and concentration $c = \bar{c} + c'$. Total vertical mass flux was calculated by combining the turbulent flux ($w'c'$) and diffusive flux ($-D\partial\bar{c}/\partial z$). Flux to the sediment-water interface computed just above the viscous boundary layer and linearly extrapolated to the bed surface at $z = 0$ cm.

3. Results

3.1. Velocity and Turbulence Structure

[16] Mean velocities and relevant turbulence characteristics for all experiments are given in Table 1, while vertical profiles of horizontal velocities and turbulent Reynolds stresses ($\overline{u'w'}$) are shown in Figure 4. In general, an increase in bed roughness increases the ratio of turbulence to mean velocity within the boundary layer flow. Both the sand and gravel bed show a distinct logarithmic velocity profile throughout the outer region of the bottom boundary layer. For the cobble bed geometry, velocity and turbulence structure was measured above and downstream of an individual cobble, where a shear layer formed due to flow separation over the top of the cobble and a peak in turbu-

lence occurred at an elevation of $z/H = 0.1$. This flow structure resembles that of a plane-mixing layer, which is characterized by an inflection in the mean velocity profile.

[17] Friction velocities u_* and bed roughness length scales z_o for the three bed geometries were computed using equation (1). The elevation of the sand bed was set to $z = 0$ cm and had no vertical offset ($d_o = 0$ cm). Since gravel and cobbles were added over the sand layer, increasing the elevation of the bed $d_o = 0.25$ cm was assigned for these two bed geometries. A logarithmic fit to the velocity profile for the cobble bed was obtained only for flow above the shear layer region, indicating a spatially averaged friction velocity.

[18] In reality, the cobbles were widely spaced, creating isolated roughness elements, and local bed shear stresses were highly variable and dependent upon the location of the bed with respect to the roughness elements. When topographic roughness becomes very large estimates of u_* using equation (1) may not adequately quantify local shear stresses at the bed ($\tau = \rho u_*^2$) due to the formation of a shear layer located within the region near the top of the roughness elements [Schlichting and Gersten, 2000]. In such cases, an independent estimate of the friction velocity can be obtained through direct computation of the total shear stress by summing the viscous and the turbulent components of stress. Within a well-developed open channel flow, the total shear stress takes the form [Nezu and Nakagawa, 1993; Stacey et al., 1999],

$$\tau = \mu \frac{\partial \bar{u}}{\partial z} - \rho \overline{u'w'} = \rho u_{*rs}^2 \left(1 - \frac{z}{H}\right). \quad (8)$$

In the above equation, the total stress = viscous “+” turbulent stresses, where $-\rho \overline{u'w'}$ is the local Reynolds or turbulent stress. Estimates of u_{*rs} were made using measurements of $\overline{u'w'}$ and $\partial \bar{u} / \partial z$ at $z/H = 0.1$, where the vertical distribution of Reynolds stresses are relatively constant. Values are given in Table 1 and indicate that u_{*rs} estimates from Reynolds stresses are within 10%–20% of those estimates computed using equation (1). This relative agreement is similar to that found by Rippeth et al. [2002] in a channel flow.

[19] Overall, for a given bed roughness, as the velocity of the mean flow increases, u_* increases without a statistical change in z_o . As bed geometry becomes more rough, both u_* and z_o increase for similar mean flow conditions. The coefficient of drag (C_D) can be computed using the equation [Kundu, 1990],

$$C_D = \frac{u_*^2}{U_o^2}, \quad (9)$$

where U_o is the time-averaged longitudinal velocity at $z/H = 0.25$. For the sand bed, $C_D = 0.003 \pm 0.001$, which is the same as the canonical value often used for flows over relatively smooth sand or mud beds [Gross and Nowell, 1983]. $C_D = 0.008 \pm 0.002$ was estimated for flows over the gravel bed, while for the cobble bed, $C_D = 0.018 \pm 0.004$, indicating the enhanced drag with rougher bed topographies.

3.2. Scalar Flux

[20] The turbulent flux of mass $\overline{w'c'}$ was locally measured for every 8×8 pixel subwindow. The vertical mass flux is shown in Figure 5, which indicates a high degree of variability both throughout the boundary layer and at different

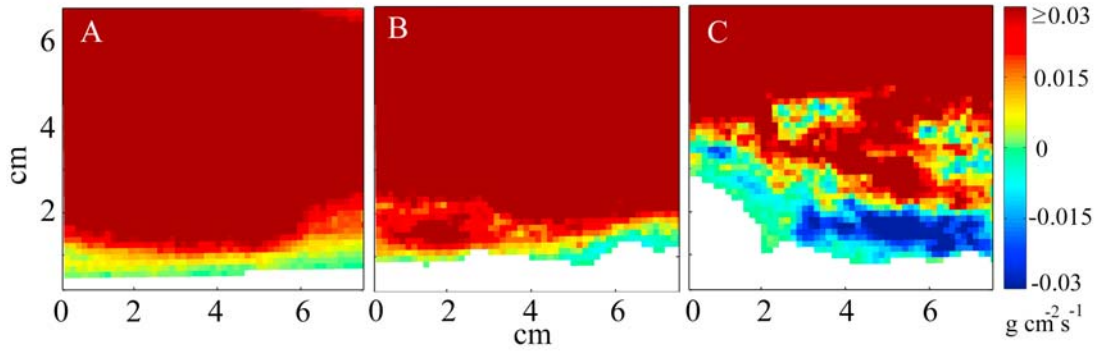


Figure 5. Turbulent flux ($\overline{w'c'}$) above the (a) sand, (b) gravel, and (c) cobble bed topography.

locations along the sediment-water interface. Since the source concentration was located 1 m upstream and along the bed, the majority of vertical flux is positive, indicating upward transport away from the bed. Within a narrow region adjacent to the bed, the flux is negative, indicating downward transport of mass toward the sediment. Estimates of turbulent flux to the sediment-water interface were computed using measurements obtained within the water column between 1 and 5 mm above the bed. Scaling arguments suggest that these measurements are at a nondimensional height ($z^+ = u_*z/\nu$) between $z^+ = 4\text{--}20$ for the sand, $z^+ = 6\text{--}30$ for the gravel, and $z^+ = 8\text{--}50$ for the cobble bed. However, since the bed is composed primarily of permeable sediments, it is likely that high-energy turbulent eddies could penetrate into the upper sediment layer, down to a few sediment grains thick [Nagaoka and Ohgaki, 1990]. The gradient in the turbulent flux was typically constant in this region and turbulent flux at $z^+ = 0$ was estimated through a linear extrapolation to the bed. Across this same elevation, the diffusive flux was also computed using equation (2), where $\partial c/\partial z$ was estimated as the temporal average over 5000 PLIF images for each experimental condition. Mean total flux estimates for each experiment are shown in Table 2. Measurements indicate that the flux due to turbulent processes is typically 1–2 orders of magnitude larger than diffusive processes. This is not surprising since at the outer edge of the viscous sublayer gradients in concentration are typically much weaker than within the viscous sublayer, reducing the impact of diffusive flux relative to turbulent processes. The relative magnitude of turbulent to diffusive flux increased with increasing bed roughness, likely due to a

combination of enhanced turbulent mixing and an overall reduction in the thickness of the viscous sublayer. Total flux also increased with increasing mean flow.

[21] The bed roughness and velocity also had a significant influence on the distribution of concentration fluctuations within the bottom boundary layer. Profiles of the mean and standard deviation of the concentration fluctuations, measured as $\sigma_c = \sqrt{c'^2}$, are shown in Figure 6. The mean profile is fairly uniform throughout the boundary layer down to the region near the top of the viscous sublayer. The standard deviation however shows marked changes from the mean profile. Enhanced bed roughness increases concentration homogeneity near the bed, as indicated by a decrease in the standard deviation of concentration.

[22] Estimates of β were computed from equation (3) using measured flux estimates and the difference between the concentration within the bulk flow c_∞ and the concentration at the sediment-water interface c_o . Solute concentration was measured on the resolution of a pixel, $0.17\text{ mm} \times 0.17\text{ mm}$. c_o was estimated by determining the location of the sediment-water interface using edge detection software and taking the average of the concentrations measured 0.17 mm above the interface. Determination of c_o by this method is likely an overestimate since measurements slightly above the interface are used, incorporating errors in the estimate of β by up to 10%. c_∞ was calculated as the average concentration above the viscous sublayer, between $z/H = 0.01$ and 0.05 . Values for β , c_∞ , and c_o are given in Table 2.

[23] Increases in β occur with increasing mean velocity and bed roughness, as expected. The relative enhancement of β by bed topography can be estimated by a comparison

Table 2. Mass Flux Characteristics for the Sand, Gravel, and Cobble Bed Geometry Experiments^a

| Experiment | U_o (cm s^{-1}) | Turbulent Flux ($\mu\text{g cm}^{-2} \text{s}^{-1}$) | Diffusive Flux ($\mu\text{g cm}^{-2} \text{s}^{-1}$) | Turbulent/Diffusive Flux | β ($\times 10^{-3}$) (cm/s) | β_{smooth} ($\times 10^{-3}$) (cm/s) | $\beta/\beta_{\text{smooth}}$ | c_o ($\mu\text{g cm}^{-3}$) | c_∞ ($\mu\text{g cm}^{-3}$) |
|------------|---------------------------------|-----------------------------------------------------------|-----------------------------------------------------------|-----------------------------|---------------------------------------------------|--------------------------------------------------------|-------------------------------|------------------------------------|-----------------------------------------|
| S1 | 6.8 | -2.6×10^{-4} | -1.1×10^{-5} | 23.7 | 0.17 | 0.13 | 1.3 | 0.20 | 1.77 |
| S2 | 8.9 | -3.4×10^{-4} | -1.1×10^{-5} | 31.2 | 0.23 | 0.17 | 1.4 | 0.29 | 1.79 |
| S3 | 11.2 | -5.7×10^{-4} | -1.3×10^{-5} | 44.1 | 0.32 | 0.22 | 1.5 | 0.31 | 2.08 |
| G1 | 5.9 | -1.9×10^{-3} | -4.5×10^{-5} | 43.6 | 0.49 | 0.19 | 2.5 | 0.43 | 4.46 |
| G2 | 7.1 | -2.2×10^{-3} | -3.7×10^{-5} | 61.1 | 0.62 | 0.23 | 2.7 | 0.31 | 3.95 |
| G3 | 9.0 | -3.2×10^{-3} | -2.9×10^{-5} | 110.3 | 0.82 | 0.28 | 2.9 | 0.31 | 4.20 |
| C1 | 5.5 | -8.1×10^{-3} | -3.4×10^{-5} | 237.6 | 2.02 | 0.28 | 7.2 | 0.65 | 4.66 |
| C2 | 6.8 | -1.0×10^{-2} | -3.1×10^{-5} | 332.3 | 2.56 | 0.34 | 7.5 | 0.56 | 4.46 |
| C3 | 8.0 | -7.9×10^{-3} | -2.6×10^{-5} | 306.5 | 2.23 | 0.34 | 6.6 | 0.42 | 3.95 |

^a β is the mass transport coefficient measured from direct estimates of the sum of the turbulent and diffusive flux, using equation (5). β_{smooth} is the estimate for hydraulically smooth bed conditions, using equation (4). c_o and c_∞ are the wall and bulk solute concentrations, respectively.

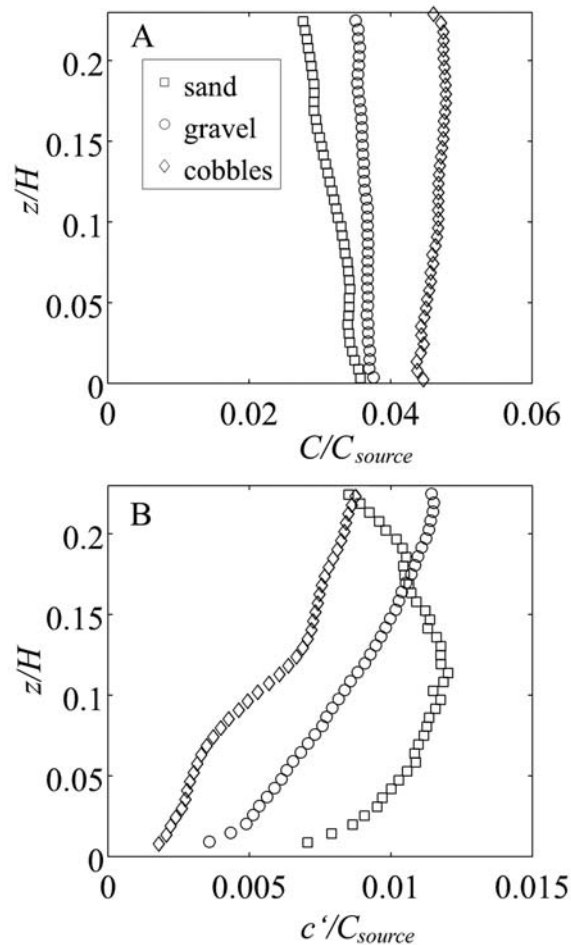


Figure 6. Vertical profiles of (a) average concentration and (b) standard deviation of the concentration fluctuations for the intermediate flow condition (S2, G2, and C2).

to the flat bed empirical relationship of the mass transfer coefficient using equation (4). Enhancement rates are shown in Figure 7 as a function of the roughness Reynolds number, $Re_* = u_* d_g / \nu$, where d_g is the mean sediment diameter and ν is the kinematic viscosity of water, $\nu = 1.005 \times 10^{-2} \text{ cm}^2 \text{ s}^{-1}$ at 20°C . The relative enhancement of β due to topography varies between 1.3 times greater for the sand bed up to 7.5 times greater for the cobble bed. The flat bed empirical relationships β_{smooth} were formed under the assumption of a hydraulically smooth boundary. Flow is typically considered hydraulically smooth when the roughness elements are small enough to be contained within the viscous sublayer, which typically occurs when $Re_* < 5$ [Schlichting and Gersten, 2000], while for $5 < Re_* < 70$ the flow is transitionally rough, and if $Re_* > 70$ the flow is considered fully rough. However, these estimates use Nikuradse equivalent sand grain roughness (k_s) instead of mean sediment diameter to estimate Re_* . For flows over beds of densely packed uniform sand grains, d_g is roughly equivalent to k_s , but for larger roughness, k_s is a function of the diameter, shape, and spacing of roughness elements. For bed geometries of gravel and cobbles, an approximate relationship reported by Schlichting and Gersten [2000] is $k_s \sim 1/3 d_g$, which in-

dicates bed geometries tested span the range between smooth to fully rough.

3.3. Quadrant Analysis

[24] Quadrant analysis is a useful technique to describe how the turbulent fluctuations contribute to momentum distribution throughout the bottom boundary layer [Lu and Willmarth, 1973; Luchhik and Tiederman, 1988]. To perform quadrant analysis, u' and w' velocity fluctuations are divided into four quadrants based on the sign of their instantaneous values. Contours of the turbulent probability distribution function (pdf) are shown in Figure 8 for turbulent motions 5 mm ($z/H = 0.02$) above the sediment surface and approximately 6 cm downstream from the leading edge of the imaging area. In quadrant 1 (Q1), $u' > 0$, $w' > 0$; in Q2, $u' < 0$, $w' > 0$ (a turbulent ejection); in Q3, $u' < 0$, $w' < 0$; and in Q4, $u' > 0$, $w' < 0$ (a turbulent sweep). Sweeping events, as indicated by pdf values in Q4, transport high-momentum fluid downward toward the sediment. Conversely, pdf values in Q2 indicate ejection of low-momentum fluid vertically upward away from the bed. These ejection-sweep phenomenon results in intermittent flushing of “dead water” that accumulates among roughness elements [Grass, 1971]. Typically, momentum transport is dominated by these ejection and sweeping events and show a predominance of values in Q2 and Q4. This is true for all three bed geometries. For the sand bed, vertical velocity fluctuations are very small, and most of the motion is due to horizontal fluctuations u' . As the bed topography becomes more rough, the intensities of the ejections and sweeps become stronger. Enhanced vertical transport of momentum toward the bed occurs with increasing roughness, as indicated by the change in slope of the pdf. For the sand and gravel bed, $w' < u'$, while for the cobble bed, the turbulence becomes nearly isotropic, with $w' \sim u'$. No statistically significant variations were found between motions in Q2 versus Q4, indicating that ejection and sweeping events were roughly equal in each of the three bed topographies adjacent to the bed.

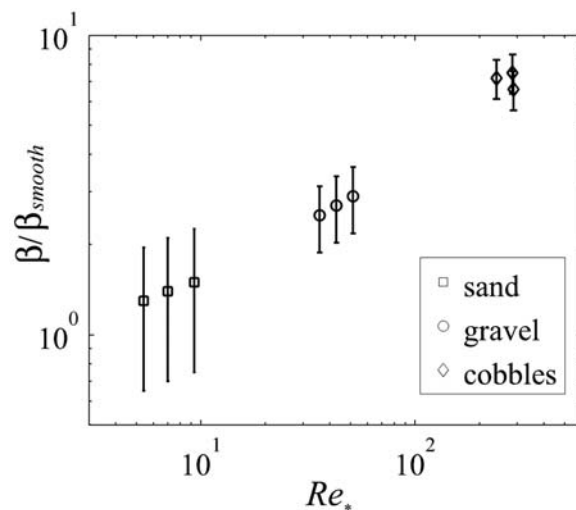


Figure 7. Mass transfer enhancement over flat bed estimates (β/β_{smooth}) as a function of the roughness Reynolds number Re_* .

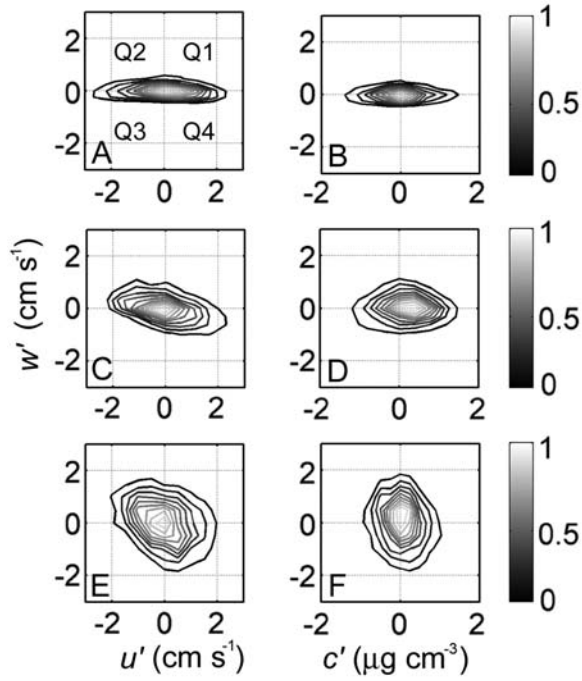


Figure 8. Quadrant analysis of the probability density functions (pdfs) of u' and w' distributions at 5 mm above the bed for the (a) sand, (c) gravel, and (e) cobble bed at the intermediate flow condition (S2, G2, and C2). Large ejection and sweeping events occur, as indicated by a greater fraction of stress occurrences within quadrants 2 and 4. Quadrant analyses of the pdfs of c' and w' distributions for the same location are shown for the (b) sand, (d) gravel, and (f) cobble bed topography. Ejection-sweeping events become more dominant with increasing bed roughness, coinciding with a consistently smaller magnitude of c' and larger magnitude of w' .

[25] In a similar fashion, probability contours of the w' versus c' can be obtained, indicating ejection and sweep motions of mass: in Q1, $c' > 0$, $w' > 0$; in Q2, $c' < 0$, $w' > 0$ (an ejection away from the bed); in Q3, $c' < 0$, $w' < 0$; and in Q4, $c' > 0$, $w' < 0$ (a sweep toward the bed). At $z/H = 0.02$, over the sand no dominant motions are evident in any quadrant indicating that ejection-sweep phenomenon is not a major factor in mass flux and the total overall flux is small. For the gravel and cobble bed, there begins to emerge the dominance of motion in Q2 and Q4 indicating a vertical flux of mass toward the bed. Two characteristics that emerge are increased vertical turbulent motions (i.e., greater w') and increased concentration homogeneity (i.e., smaller c') with increasing bed roughness. This indicates that, as the boundary layer becomes more rough, turbulent motions are increased, which enhance mixing and create a more uniform concentration distribution. In a similar fashion to the Reynolds stress measurements, Q2 and Q4 contributions were greater than Q1 and Q3, but the relative magnitude of ejection and sweeping events were statistically similar.

[26] The efficiency of momentum transport is measured through the correlation coefficient, $r_{uw} = \frac{\overline{u'w'}}{\sigma_u \sigma_w}$, where σ_u and σ_w are the standard deviations of u and w , respectively. Within the constant stress layer, sand (S2) and gravel (G2)

topographies have a value of $r_{uw} = -0.32$ and $r_{uw} = -0.33$, respectively. This matches typical values found in the inertial sublayer for a variety of atmospheric boundary layers [Raupach *et al.*, 1996]. In contrast, for the cobble bed geometry (C2), values for r_{uw} peak at -0.56 in the shear layer within the wake of the cobble, while within the upper boundary layer, a relatively uniform value of -0.33 occurs. The increase in magnitude of r_{uw} indicates that the turbulence near the mixing layer formed in the wake of the cobble is much more efficient in the transport of momentum than the flow above.

3.4. Turbulent Kinetic Energy

[27] The turbulent kinetic energy (TKE) budget for flow can be expressed as [Townsend, 1976]

$$\bar{u} \frac{\partial(\overline{0.5q^2})}{\partial x} + \bar{w} \frac{\partial(\overline{0.5q^2})}{\partial z} = -\overline{u'w'} \frac{\partial U}{\partial z} - \frac{\partial(\overline{0.5q^2 w'})}{\partial z} - \frac{1}{\rho} \frac{\partial(\overline{w'p'})}{\partial z} - \varepsilon, \quad (10)$$

where overbars signify time-averaged quantities, ρ is density, p is pressure, and $q^2 = \overline{u'u'} + \overline{v'v'} + \overline{w'w'}$ is turbulent kinetic energy. Since the $\overline{v'v'}$ component was not measured, the TKE was modeled as $q^2 = \overline{u'u'} + 2.3(\overline{w'w'})$. The factor of 2.3 was used since a general feature of boundary shear layers is that the relative intensities of the three components of velocity are much the same with $\overline{v'v'}$ being approximately equivalent to $1.3\overline{w'w'}$ [Raupach *et al.*, 1991]. In a fully developed boundary layer, the advective terms on the left in equation (10) are equal to zero, and on the right, the largest terms are production $P = -\overline{u'w'} \frac{\partial U}{\partial z}$ and dissipation ε . Under equilibrium conditions, these terms tend to be in balance and the other terms are negligible. Under nonequilibrium conditions, TKE is transported, either through turbulent transport (T_t) or pressure driven transport (T_p), the second and third terms on the right-hand side of equation (10), respectively. TKE production, dissipation, and turbulent transport can be measured directly, while the pressure transport term is typically not measured but is set equal to the residual of the other terms [Finnigan, 2000].

[28] Dissipation of TKE was determined through direct measurements of the ensemble average of the strain rate [Tanaka and Eaton, 2007],

$$\varepsilon_D = 2\nu \langle S_{ij} S_{ij} \rangle \quad (11)$$

where ν is the kinematic viscosity, S_{ij} is the strain rate, and the brackets $\langle \rangle$ denote ensemble average. TKE dissipation was computed using a second-order central difference approximation. Since the out-of-plane component is not available, we multiply the in-plane contribution by 15/7 to account for the out-of-plane contribution, assuming isotropic, homogeneous turbulence [Fincham *et al.*, 1996]. The resulting expression is [Zhu *et al.*, 2006]

$$\varepsilon_D = \frac{15}{7} \nu \left[2 \left\langle \frac{\partial u^2}{\partial x} \right\rangle + 2 \left\langle \frac{\partial w^2}{\partial z} \right\rangle + \left\langle \frac{\partial u^2}{\partial z} \right\rangle + \left\langle \frac{\partial w^2}{\partial x} \right\rangle + 2 \left\langle \frac{\partial u}{\partial z} \frac{\partial w}{\partial x} \right\rangle \right]. \quad (12)$$

For the sand (Figure 9) and gravel bed (not shown), a general balance occurs between P and ε , with minimal transport of

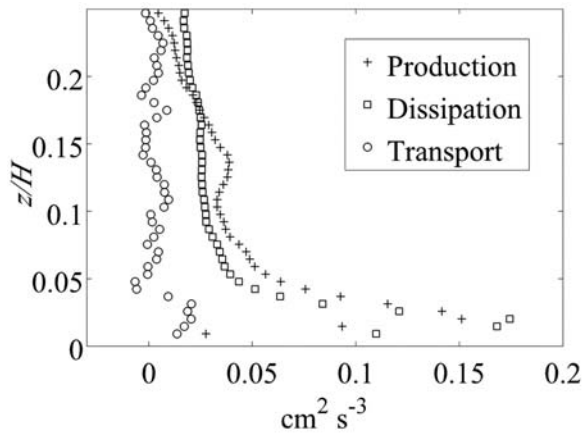


Figure 9. Turbulent kinetic energy production, dissipation, and transport for flow over the sand bed (S1).

TKE, indicating equilibrium conditions throughout the BBL. For the cobble bed, the shear layer region formed in the wake of a cobble has very active mixing and extremely large production rates (Figure 10). This production is not balanced locally by dissipation (as evident by comparisons between plots of P and ϵ). Turbulent transport, along with the residual pressure transport, is large in this region and redistributes the TKE away from the shear layer, with a loss in T_t near the top of the shear layer region where P peaks and a gain lower within the recirculation zone of the wake. These shear layer dynamics within the wake behind individual roughness elements enhance vertical exchange of mass and momentum, as evident by an increased magnitude of r_{uw} and increased turbulent interaction with the bed. Dissipation rate estimates for all experiments are listed in Table 1 at an elevation $z/H = 0.1$. Using dissipation measurements at this elevation, the Kolmogorov length scale η , which is the smallest scale of turbulent motion, can be computed as $\eta = \left(\frac{\nu^3}{\epsilon}\right)^{1/4}$ (Table 1).

3.5. Pore Water Concentrations

[29] To determine how this vertical flux effects sediment pore water concentrations, water samples were taken 0.5 cm

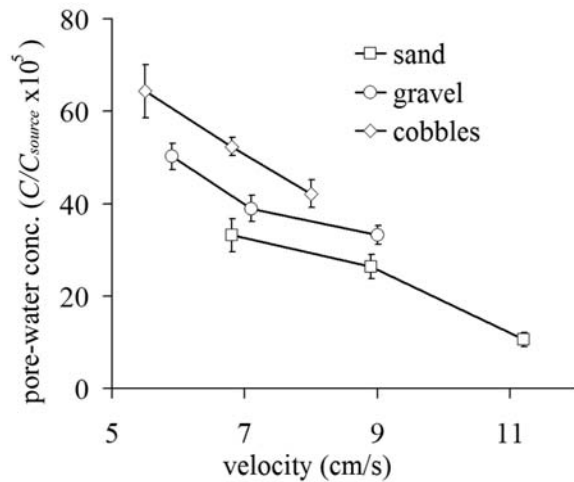


Figure 11. Pore water concentration as a function of mean velocity for the three different bed topographies.

below the sediment surface, directly beneath the PLIF/PIV imaging area. Increased pore water concentrations occurred with increasing bed roughness (Figure 11), which correlates well to the observed increase in flux to the sediment-water interface. However, decreased pore water concentrations were found with increased water column velocities for a given bed roughness, opposite that suggested from local flux measurements. Flow-sediment interaction produces drag as a resistance to the flow. Since the bed is permeable, variations in pressure head along the bed surface can create horizontal and vertical advective flow through the porous bed material [Elliot and Brooks, 1997b]. Although not directly measured, the observed trend of reduced pore water concentration with increased velocity is likely a result of enhanced dispersion and downstream advective transport of the solute through the sediment layer.

4. Discussion

[30] Mass flux to and from aquatic sediments has traditionally been measured using steady state concentration

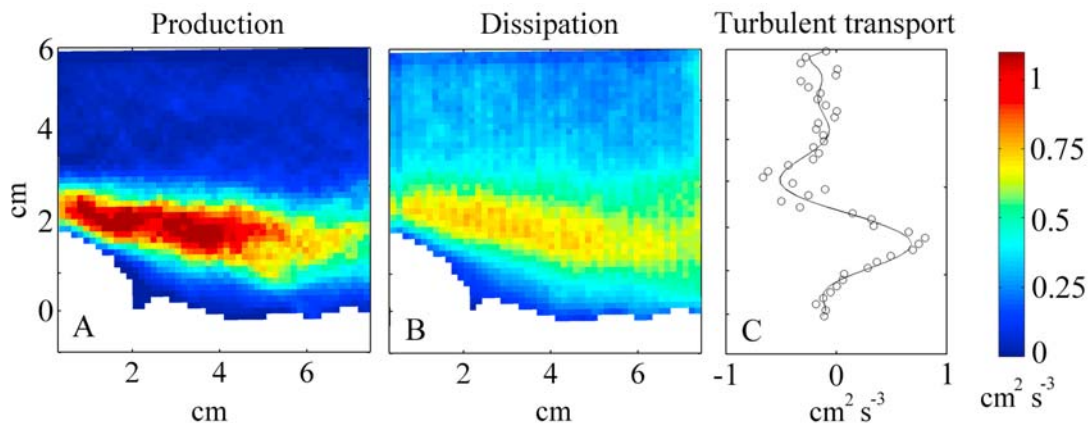


Figure 10. (a) Production, (b) dissipation, and (c) turbulent transport for the cobble bed geometry (C2). Large transport of TKE occurs in the wake region behind the cobble.

profiles adjacent to and within bed sediments where gradient diffusion theory can be applied. Typically, this has been done since direct and simultaneous measurements of concentration and velocity at a single location have been difficult to obtain. The transport rate is due to complex interactions of diffusion, advection, shear, and turbulence that create large variations in chemical residence times [O'Connor and Harvey, 2008]. In this study, we utilized two complimentary techniques, planar laser-induced fluorescence to measure solute concentration, and particle image velocimetry to measure fluid motion adjacent to the sediment-water interface without disturbing the sediment or flow structure. The measurements reveal that variations in bottom topography can substantially affect rates of turbulent mixing throughout the bottom boundary layer and mass flux to the sediment-water interface.

4.1. Scalar Flux

[31] Directly adjacent to the sediment-water interface, for all bed and flow conditions, a negative flux occurred, indicating input of mass from the water column into pore waters of the bed sediments. The distribution of negative flux grows in the vertical extent with increasing bed roughness, primarily due to the increase in turbulent interaction with the bed. Scaling of the flux by $c_\infty - c_o$, the mass transfer coefficient β approximately doubles with an increase in roughness from a sand to gravel topography and increases by an order of magnitude between the sand and cobble bed geometries. Increases in topography not only affect bed shear stress and therefore u_* but also the turbulent structure within the bottom boundary layer. Flow over the sand bed was found to be hydraulically smooth, and direct estimates of β matched well that predicted using smooth bed theory. For transitionally rough or fully rough bed conditions, mass transfer enhancements over smooth bed estimates were found through enhanced turbulent interactions between the bed and the overlying flow.

[32] Direct impacts of roughness heights on flux into sandy sediments were measured by Huettel *et al.* [1996] who found roughly a doubling of the exchange flux with a fivefold to tenfold increase in the roughness height. Our measurements find similar results when comparing sand to gravel grain sizes. When extended to roughness length scales on the height of a cobble, an approximate tenfold increase in flux for a 100-fold increase in bed roughness was measured. Packman and Salehin [2003] summarized a number of studies of exchange rates across different sediment types ranging from fine sand to gravel and expanded upon the theoretical framework and two-dimensional model for advective exchange processes developed by Elliot and Brooks [1997a] for flow over dune-shaped bed forms. Although these models cannot necessarily be expected to apply directly to natural streams or to bed conditions measured in this study due to the range of different bed features, they are useful to parameterize the relative roles of stream and sediment conditions in controlling fluxes across the sediment-water interface. The effective diffusion coefficient D_e for exchange across the sediment-water interface has been shown using these models and laboratory experiments to be linearly proportional to the parameter grouping Kh_m/θ and holds for more than three orders of magnitude

of bed form driven exchange [Packman and Salehin, 2003], where

$$\frac{Kh_m}{\theta} = 0.28 \frac{K}{\theta} \frac{U^2}{2g} \left(\frac{d/H}{0.34} \right)^{3/8} \quad d/H < 0.34. \quad (13)$$

The parameters hydraulic conductivity K and porosity θ characterize the sedimentary control on bed form driven exchange, while h_m reflects the half-amplitude of the sinusoidal bed form induced pressure variation at the bed surface. Equation (13) includes the bed form height d to water depth H ratio and indicates the driving mechanism for advective exchange includes the stream velocity, sediment characteristics K and θ and a geometric term related to the bed form shape. Application of this model, in combination with laboratory experiments, indicated that sinusoidal shaped bed forms with heights between 2.2 and 3.7 cm consistently increased exchange by a factor of 3–6 [Packman *et al.*, 2004]. Although the Elliot and Brooks [1997a] model cannot be directly applied to our experiments due to the random arrangement of bed roughness elements, we found similar but slightly larger enhancement (up to 10 times) when comparing a smooth sand bed and one composed of ~3 cm high cobble roughness elements. Enhancement above theoretical predictions and measurements over two-dimensional bed forms may likely be caused by the three-dimensional flows and pressure distributions created by the irregular bed forms, as suggested by Elliot and Brooks [1997b].

[33] Bed topography also affected both the distribution and magnitude of flux along the bed. Roughness elements, if large enough to protrude through the viscous sublayer, created heterogeneous shear at the bed, which altered local rates of mass exchange. This phenomenon has been observed even over small-scale sediment topography with millimeter-scale variations, affecting the transport rate of oxygen across the diffusive boundary layer [Roy *et al.*, 2002]. The substantially larger roughness measured here and found in many river systems enhances the heterogeneous exchange and creates local hot spots for flux of dissolved and particulate matter. These hot spots correlate with regions of boundary layer separation and reattachment along the bed. The dominant feature of the flow near the bed in the cobble flow is the region of strong shear, creating an inflection point near the top of the cobble in the mean velocity and large coherent vortices that form in the wake. Similar characteristics, although not as pronounced, are evident over the gravel bed, where flow separation occurs behind individual gravel elements, creating variability in the magnitude of flux along the bed. This spatial intermittency denotes the inherent difficulty of measuring flux over naturally rough surfaces through gradient-diffusion estimates using profiles of concentration at one location.

4.2. Velocity and Turbulence Structure

[34] For relatively uniform distribution of roughness elements, such as that of the sand and gravel bed, the flow profile and turbulence structure typically followed that of a logarithmic bottom boundary layer. As bed roughness increased to that dominated by cobbles, turbulent mixing processes were driven by shear flow over the protruding

structures, resulting in boundary layer flow separation around individual roughness elements and the shedding of vortices in the wake region downstream of the protrusion. Within a turbulent boundary layer, kinetic energy from the free streamflow is converted to turbulent motions that are dissipated into internal energy by viscous action [Robinson, 1991]. This process is continual, and therefore, to be self-sustaining, there must be a balance of turbulence generation and dissipation. Where turbulence is produced and where it is dissipated depends upon the dynamics contained within the internal structure of the boundary layer flow. A balance between production and dissipation of TKE was found throughout the majority of the bottom boundary layer for the sand and gravel beds. Over the cobble bed, the shear layer produced very active local mixing and large production rates of TKE. TKE production was not balanced locally by dissipation and thus turbulent transport, along with residual pressure transport, redistributed TKE away from the wake region and enhanced the efficiency of vertical momentum transport. The magnitude of the localized turbulence increases with roughness height relative to flow depth [Bennet and Best, 1996].

[35] The turbulent motions for all three bed conditions contain the ejection-sweep phenomenon characteristic of wall-bounded flows. The quadrant analysis examined trends of the Reynolds shear stress and the relative importance of ejection and sweep events to momentum transport. Results show that the duration and magnitude of ejections (quadrant 2) and sweeps (quadrant 4) exceed those in quadrants 1 and 3. As the bed becomes more rough, the relative contributions of ejection and sweeps to the overall turbulent motion becomes more dominant. An increase in ejection-sweep events due to increases in roughness have also been observed in atmospheric flows where spectra indicate that the strength of “active” motion depended upon boundary layer roughness [Krogstad *et al.*, 1992]. Ejection-sweep events also increased as velocity increased, and there was a relatively equal contribution of sweeps of high-momentum fluid transport toward the bed to ejections of low-momentum fluid away from the bed. Lacey and Roy [2008] found similar dominance of ejection-sweep events in the wake of pebble clusters within a natural stream which contributed to 80% of the Reynolds shear stress, although they found a dominance of ejection events. The relative magnitude of ejection and sweeping events often shifts, however, and is dependent upon such factors as the height of the protrusion, the location within the wake region and the strength of the mean flow [Sambrook Smith and Nicholas, 2005].

[36] Although ejection-sweep phenomenon has been long studied in relation to momentum transport, their importance to scalar transport is less understood [Katul *et al.*, 1997], primarily due to the difficulty in simultaneous velocity and scalar structure. Utilizing quadrant analysis, correlations between c' and w' revealed different trends than those found for correlations between u' and w' . Time-averaged Reynolds stress estimates were primarily negative due to dominant ejection-sweep phenomenon. However, the dominance of motion in Q2 and Q4 was less pronounced for mass. As the bed roughness increased, ejection-sweep motions became more dominant, increasing flux to the bed. No statistically significant difference was found in ejection or sweep events, either for momentum or mass, which was also found for

atmospheric flux measurements over plant canopies in near neutral conditions [Coppin *et al.*, 1986].

[37] Both the flow and mass transport measurements were two dimensional along an imaging area parallel to the flow. However, due to the complex bed geometry, the velocity and turbulence structure was three dimensional and likely altered mass transport and mixing both vertically and laterally across the width of the flume. The size and spacing of roughness elements will typically impact the dimension of vertical and transverse turbulent eddies that form [Hardy *et al.*, 2009], and maximum exchange rates typically occur at locations where turbulent eddies detach and reattach to the bed due to bed form-induced pressure variations [Cardenas and Wilson, 2007a, 2007b]. We conducted measurements adjacent to the large cobble roughness elements, where larger fluxes are predicted compared to spatially averaged three-dimensional measurements. However, our two-dimensional measurements are expected to predict well three-dimensional average trends occurring over the sand and gravel topography since measurements spanned many roughness elements.

[38] With the addition of the cobbles to the bed, the additional volume within the channel reduced the cross-sectional area of the flow. This reduction likely affected the overall pressure distribution along the bed, and the TKE would likely vary also due to the reduction of cross-sectional area. The cobbles had a mean height above the bed of $h = 3$ cm. Below this height, the turbulent stress gradient can be approximated as [Nepf and Vivoni, 2000]

$$\frac{\partial \overline{u'w'}}{\partial z} \cong \frac{\overline{u'w'}}{h}, \quad (14)$$

assuming the turbulent stress penetrates to the bed, while the momentum balance of the flow above the cobbles is

$$\overline{u'w'}|_h = g \frac{\partial H}{\partial x} (H - h). \quad (15)$$

Substituting (15) into (14), the ratio of the pressure gradient to the turbulent stress gradient beneath the height of the cobbles is

$$\frac{\text{turbulent stress}}{\text{pressure}} = \frac{\partial \overline{u'w'} / \partial z}{g \partial H / \partial x} \cong \frac{H}{h} - 1. \quad (16)$$

For the case of the cobble flow, the turbulent stress to pressure ratio would be $0.25/0.03 - 1 = 7.3$, indicating that, while turbulent stress is still dominant, pressure-driven flow dynamics become more important with larger overall roughness for a given water depth.

4.3. Scaling of the Diffusive Boundary Layer Thickness

[39] Estimates of the mass transfer coefficient β indicate enhancements up to 7.5 times greater than equivalent smooth beds. This increase is due to alteration of fluid shear and turbulence intensity near the bed, which acts to transport mass more efficiently to the sediment-water interface and reduce the thickness of the diffusive boundary layer. Since direct measures of the diffusive sublayer thickness were not made, a useful scaling, which has been proposed by Hearn and Robson [2000], uses the Batchelor length scale $L_B = 2\pi \left(\frac{\nu D^2}{\varepsilon} \right)^{1/4}$ to approximate δ . The Batchelor length

scale describes the smallest length scale of the turbulent fluctuations of the solute concentration, which occur before molecular diffusion smoothes the remaining concentration fluctuations. Since the viscous sublayer is defined as the region of fluid next to a solid surface where turbulence is suppressed and molecular diffusion dominates transport of solute, a similar argument can be made for using the Batchelor length in defining the thickness of the DSL [Lorke *et al.*, 2003; O'Connor and Hondzo, 2008]. Using dissipation measurements within the inertial range of the bottom boundary layer, values for δ estimated through the Batchelor length scale range between $\delta = 1.1 \times 10^{-2}$ cm for the sand bed to $\delta = 5.0 \times 10^{-3}$ cm for the cobble bed. Utilizing thin film theory, the mass transfer coefficient can be estimated as $\beta = D/\delta$. Values for β range from 4.7×10^{-4} cm/s to 1.0×10^{-3} cm/s, which match general estimates of β through direct flux measurements for the sand bed but tend to under predict flux as the bed becomes topographically more rough. This is not surprising given that thin film theory assumptions of a uniform, equilibrium boundary layer tend to become invalid as the flow transitions from smooth to transitional to fully rough. Additionally, since the bed is permeable, enhanced turbulent interaction with the bed should augment the ability for turbulent motions to penetrate through the top of the sediment layer, increasing transport of mass into the sediment pore waters.

4.4. Pore Water Concentrations

[40] Theoretical prediction of mass transfer for turbulent flows indicate that rates of mass transfer should be proportional to u_* over smooth beds, since the shear stress velocity controls the diffusive sublayer thickness [Hondzo, 1998]. For a steady flow to be maintained, the frictional resistance caused by the bed must be balanced by a counteracting pressure gradient. This pressure gradient is formed by a sloping water surface, and since this slope is a large-scale phenomenon the pressure gradient can penetrate a considerable distance into the bed, creating an interstitial underflow [Elliot and Brooks, 1997a]. In addition, local flow interaction with individual roughness elements produces drag against the flow and variations in pressure form both within the boundary layer and in the pore waters even due to minor topographic variations in the bed topography [Elliot and Brooks, 1997b]. With increasing water column velocities and/or increasing roughness heights, increases in pore water velocities and subsurface transport occur [Huettel and Gust, 1992]. This interaction is consistent with advective pumping theory for flow within bed sediments, which suggest that any topographical feature that induces flow separation should increase exchange relative to smooth beds [Packman *et al.*, 2004]. Therefore, pore water concentrations are dependent both upon the vertical flux due to turbulent exchange processes within the water column and horizontal and vertical pore water flow through the subsurface sediment layer. Our results are consistent with predicted theory that increased roughness increases turbulent exchange between the water column and the pore waters, enhancing pore water concentrations. However, our measurements also indicated reduced pore water concentrations with increased mean flow. Although not measured, this was likely caused by enhanced subsurface flow and downstream

transport and dispersion of chemicals through the permeable sediments, reducing pore water concentrations at the measurement location. Adjacent to the bed, momentum in the overlying flow can also penetrate to the upper layers of sediment causing both increased dispersion and downstreamflow above that of the underlying Darcy-type flow. The velocity in this layer, often referred to as Brinkman velocity or slip velocity, has been found to be proportional to the velocity gradient in the overlying flow [Beavers and Joseph, 1967] and appears to develop rather quickly to a layer thickness that is on the order of the grain size diameter [Goharzadeh *et al.*, 2005]. Due to the shallow depth of the sediment layer, this Brinkman flow may also have exerted a large impact on enhancing overall bulk flow through the porous bed. Future measurements of coupled above and below water fluxes will be needed, similar to numerical simulations conducted by Cardenas and Wilson [2007b], to determine how subsurface flow and dispersion processes are linked to water column hydrodynamics.

4.5. Hydrologic Exchange and Biogeochemical Processes

[41] The hyporheic zone at the sediment-water interface is an important region for the exchange of water masses containing dissolved nutrients and gases, which are vital for both benthic fauna and aquatic macrophytes [Nepf and Koch, 1999]. The uptake of these chemicals depends upon physical, as well as biological and geochemical, processes. This study did not involve any active geochemical or biological uptake and physical transport processes solely controlled transfer across the sediment-water interface. In natural systems however, nutrient uptake by stream periphyton is controlled by a combination of mass transfer through the DSL and by kinetic transfer through cell membranes into cells [Jumars *et al.*, 2001]. Flow conditions act as an important regulator for exchange processes, where mass transfer control is expected at low velocities, when the DSL is thick, with kinetic control at higher velocities, but when the DSL becomes so thin, diffusional transport through it is faster than membrane transport [Larned *et al.*, 2004]. Hydrodynamic transport conditions were also found to play a key role in structuring benthic microbial communities, both in terms of total biomass and in taxonomic composition [Arnon *et al.*, 2007]. At high velocities, shear stress and turbulence was found to influence biofilm growth and metabolism [Hondzo and Wang, 2002], but even under slow flow conditions where shear stresses are minimal, flow variations produce differences in nutrient supply rates to the benthos, altering community structure [Arnon *et al.*, 2007]. These structural differences regulate microbial processing of nutrients supplied from the water column and increased bed roughness should only enhance variability in benthic biomass and microbial communities.

[42] In conclusion, bed roughness was found to substantially enhance both the magnitude and spatial variability of momentum and mass flux due to altering bed shear stresses, TKE balances, and turbulent flow dynamics adjacent to the bed. A better understanding of these relationships improves our ability to predict and quantify nutrient retention and utilization in streams and further illustrates how hydrodynamics can play a critical role in benthic ecology.

[43] **Acknowledgments.** We thank Mimi Koehl for the use of her planar laser-induced fluorescence system (James S. McDonnell Foundation award 21002091), Rudi Schuech for his assistance with the experiments, and Peter Berg for his helpful comments and suggestions. This project was supported by a fellowship from the Miller Institute for Basic Research in Science to M.A.R. and from the National Center for Earth Surface Dynamics to M.L. and M.H.

References

- Antonia, R. A., and R. E. Luxton (1971), The response of a turbulent boundary layer to a step change in surface roughness: Part 1. Smooth to rough, *J. Fluid Mech.*, *48*, 721–761.
- Amon, S., A. I. Packman, C. G. Peterson, and K. A. Gray (2007), Effects of overlying velocity on periphyton structure and denitrification, *J. Geophys. Res.*, *112*, G01002, doi:10.1029/2006JG000235.
- Battin, T. J., L. A. Kaplan, J. D. Newbold, and C. M. E. Hansen (2003), Contributions of microbial biofilms to ecosystem processes in stream mesocosms, *Nature*, *426*, 439–442.
- Beavers, G. S., and D. D. Joseph (1967), Boundary conditions at a naturally permeable wall, *J. Fluid Mech.*, *30*, 197–207.
- Bennet, S. J., and J. L. Best (1996), Mean flow and turbulence structure over fixed ripples and the ripple-dune transition, in *Coherent Flow Structures in Open Channels*, edited by P. J. Ashworth et al., pp. 281–304, John Wiley, New York.
- Berg, P., H. Roy, F. Janssen, V. Meyer, B. B. Jørgensen, M. Huttel, and D. De Beer (2003), Oxygen uptake by aquatic sediments measured with a novel non-invasive eddy-correlation technique, *Mar. Ecol. Prog. Ser.*, *261*, 75–83.
- Berg, P., H. Roy, and P. L. Wiberg (2007), Eddy correlation flux measurements: The sediment surface area that contributes to the flux, *Limnol. Oceanogr.*, *52*, 1672–1684.
- Berger, F. P., K. F. Hau, and F. L. Hau (1979), Local mass/heat transfer distribution on surfaces roughened with small square ribs, *Int. J. Heat Mass Transfer*, *22*(12), 1645–1656.
- Boudreau, B. P., and B. B. Jørgensen (Eds.) (2001), *The Benthic Boundary Layer: Transport Processes and Biogeochemistry*, Oxford Univ. Press, New York.
- Cardenas, M. B., and J. L. Wilson (2007a), Dunes, turbulent eddies, and interfacial exchange with permeable sediments, *Water Resour. Res.*, *43*, W08412, doi:10.1029/2006WR005787.
- Cardenas, M. B., and J. L. Wilson (2007b), Hydrodynamics of coupled flow above and below a sediment-water interface with triangular bedforms, *Adv. Water Resour.*, *30*, 301–313.
- Coppin, P. A., M. R. Raupach, and B. J. Legg (1986), Experiments on scalar dispersion within a model plant canopy part II: An elevated plane source, *Boundary Layer Meteorol.*, *35*, 167–191.
- Cowen, E. A., and S. G. Monismith (1997), A hybrid digital particle tracking velocimetry technique, *Exp. Fluids*, *22*(3), 199–211.
- Dawson, D. A., and O. Trass (1972), Mass transfer at rough surfaces, *Int. J. Heat Mass Transfer*, *15*, 1317–1336.
- Elliot, A. H., and N. H. Brooks (1997a), Transfer of nonsorbing solutes to a streambed with bed forms: Theory, *Water Resour. Res.*, *33*(1), 123–136.
- Elliot, A. H., and N. H. Brooks (1997b), Transfer of nonsorbing solutes to a streambed with bed forms: Laboratory experiments, *Water Resour. Res.*, *33*(1), 137–151.
- Ferrier, A. J., D. R. Funk, and P. J. W. Roberts (1993), Application of optical techniques to the study of plumes in stratified fluids, *Dyn. Atmos. Oceans*, *20*, 155–183.
- Fincham, A. M., T. Maxworthy, and G. R. Spedding (1996), Energy dissipation and vortex structure in freely decaying, stratified grid turbulence, *Dyn. Atmos. Oceans*, *23*, 155–169.
- Finlay, J. C., M. E. Power, and G. Cabana (1999), Effects of water velocity on algal carbon isotope ratios: Implications for river food web studies., *Limnol. Oceanogr.*, *44*, 1198–1203.
- Finnigan, J. (2000), Turbulence in Plant Canopies, *Annu. Rev. Fluid Mech.*, *32*, 519–571.
- Glud, R. N., O. Holby, F. Hoffmann, and D. E. Canfield (1998), Benthic mineralization and exchange in Arctic sediments, *Mar. Ecol. Prog. Ser.*, *173*, 237–251.
- Goharzadeh, A., A. Khalili, B. B. Jørgensen (2005), Transition layer thickness at a fluid-porous interface, *Phys. Fluids*, *17*, 057102–057110.
- Grass, A. (1971), Structural features of turbulent flow over smooth and rough boundaries, *J. Fluid Mech.*, *50*, 233–255.
- Gross, T. F., and A. R. Nowell (1983), Mean flow and turbulence scaling in a tidal boundary layer, *Cont. Shelf Res.*, *2*, 109–126.
- Hardy, R. J., J. L. Best, S. N. Lane, and P. E. Carbonneau (2009), Coherent flow structures in a depth-limited flow over a gravel surface: The role of near-bed turbulence and influence of Reynolds number, *J. Geophys. Res.*, *114*, F01003, doi:10.1029/2007JF000970.
- Hearn, C. J., and J. Robson (2000), Modelling a bottom diurnal boundary layer and its control of massive alga blooms in an estuary, *Appl. Math. Model.*, *24*, 843–859.
- Hondzo, M. (1998), Dissolved oxygen transfer at the sediment-water interface in a turbulent flow, *Water Resour. Res.*, *34*, 3525–3533.
- Hondzo, M., and H. Wang (2002), Effects of turbulence on growth and metabolism of periphyton in a laboratory flume, *Water Resour. Res.*, *38*(12), 1277, doi:10.1029/2002WR001409.
- Huettel, M., and G. Gust (1992), Impact of bioirregularity on interfacial solute exchange in permeable sediments, *Mar. Ecol. Prog. Ser.*, *89*, 253–267.
- Huettel, M., W. Ziebis, and S. Forster (1996), Flow-induced uptake of particulate matter in permeable sediments, *Limnol. Oceanogr.*, *41*, 309–322.
- Jumars, P. A., J. E. Eckman, and E. Koch (2001), Macroscopic animals and plants in benthic flows, in *The Benthic Boundary Layer*, edited by B. P. Boudreau and B. B. Jørgensen, pp. 320–347, Oxford Univ. Press.
- Kader, B. A., and A. M. Yaglom (1972), Heat and mass transfer laws for fully turbulent wall flows, *Int. J. Heat Mass Transfer*, *15*(12), 2329–2351.
- Katul, G., G. Kuhn, J. Schieldge, and C. I. Hsieh (1997), The ejection-sweep character of scalar fluxes in the unstable surface layer, *Boundary Layer Meteorol.*, *83*, 1–26.
- Krogstad, P., R. Antonia, and L. Browne (1992), Comparison between rough- and smooth-wall turbulent boundary layers, *J. Fluid Mech.*, *245*, 599–617.
- Kundu, P. (1990), *Fluid Mechanics*, Academic, New York, NY.
- Lacey, J. R. W., and A. G. Roy (2008), Fine-scale characterization of the turbulent shear layer of an in-stream pebble cluster, *J. Hydraul. Eng.*, *134*(7), doi:10.1061/(ASCE)0733-9429(2008)1134:1067(1925).
- Larned, S. T., V. I. Nikora, and B. J. F. Biggs (2004), Mass-transfer-limited nitrogen and phosphorus uptake by stream periphyton: A conceptual model and experimental evidence, *Limnol. Oceanogr.*, *49*(6), 1992–2000.
- Lorke, A., B. Müller, M. Maerki, and A. Wuest (2003), Breathing sediments: The control of diffusive transport across the sediment-water interface by periodic boundary layer turbulence, *Limnol. Oceanogr.*, *48*, 2077–2085.
- Lu, S. S., and W. W. Willmarth (1973), Measurements of the structure of the Reynolds stress in a turbulent boundary layer, *J. Fluid Mech.*, *60*, 481–571.
- Luckhik, T. S., and W. G. Tiederman (1988), Turbulent structure in low-concentration drag-reducing channel flow, *J. Fluid Mech.*, *190*, 241–263.
- Nagaoka, H., and S. Ohgaki (1990), Mass transfer mechanism in a porous riverbed, *Water Resour. Res.*, *24*, 417–425.
- Nepf, H. M., and E. W. Koch (1999), Vertical secondary flows in submerged plant-like arrays, *Limnol. Oceanogr.*, *44*(4), 1072–1080.
- Nepf, H. M., and E. R. Vivoni (2000), Flow structure in depth-limited, vegetated flow, *J. Geophys. Res.*, *105*(C12), 28547–28557.
- Nezu, I., and H. Nakagawa (1993), *Turbulence in Open Channel Flows*, A. A. Balkema, Brookfield, V.T.
- Nikora, V. I., D. Goring, I. McEwan, and G. Griffiths (2001), Spatially averaged open-channel flow over rough bed, *J. Hydraul. Eng.*, *127*(2), 123–133.
- O'Connor, B. L., and J. W. Harvey (2008), Scaling hyporheic exchange and its influence on biogeochemical reactions in aquatic ecosystems, *Water Resour. Res.*, *44*, W12423, doi:10.1029/2008WR007160.
- O'Connor, B. L., and M. Hondzo (2008), Dissolved oxygen transfer to sediments by sweep and eject motions in aquatic environments, *Limnol. Oceanogr.*, *53*(2), 566–578.
- Packman, A. I., and M. Salehin (2003), Relative roles of streamflow and sedimentary conditions in controlling hyporheic exchange, *Hydrobiologia*, *494*, 291–297.
- Packman, A. I., M. Salehin, and M. Zaramella (2004), Hyporheic exchange with gravel beds: basic hydrodynamic interactions and bedform-induced advective flows, *J. Hydraul. Eng.*, *130*, doi:10.1061/(ASCE)0733-9429(2004)1130:1067(1647).
- Raupach, M., J. Finnigan, and Y. Brunet (1996), Coherent eddies and turbulence in vegetation canopies: The mixing-layer analogy, *Boundary Layer Meteorol.*, *60*, 375–395.
- Raupach, M. R., R. A. Antonia, and S. Rajagopalan (1991), Rough-wall turbulent boundary layers, *Appl. Mech. Rev.*, *44*(1), 1–25.
- Reidenbach, M. A., N. T. George, and M. A. R. Koehl (2008), Antennule morphology and flicking kinematics facilitate odor sampling by the spiny lobster, *Panulirus argus*, *J. Exp. Biol.*, *211*, 2849–2858.
- Rippeth, T. P., E. Williams, and J. H. Simpson (2002), Reynolds stress and turbulent energy production in a tidal channel, *J. Phys. Oceanogr.*, *32*, 1242–1251.

- Robinson, S. K. (1991), Coherent motions in the turbulent boundary layer, *Annu. Rev. Fluid Mech.*, *23*, 601–639.
- Roy, H., M. Huttel, and B. B. Jorgensen (2002), The role of small-scale sediment topography for oxygen flux across the diffusive boundary layer, *Limnol. Oceanogr.*, *47*, 837–847.
- Ryan, R. J., A. I. Packman, and S. Kilham (2007), Relating phosphorus uptake to changes in transient storage and streambed sediment characteristics in headwater tributaries of Valley Creek, an urbanizing watershed, *J. Hydrol.*, *336*, 444–457.
- Sambrook Smith, G. H., and A. P. Nicholas (2005), Effect on flow structure of sand deposition on a gravel bed: Results from a two-dimensional flume experiment, *Water Resour. Res.*, *41*, W10405, doi:10.1029/2004WR003817.
- Schlichting, H., and K. Gersten (2000), *Boundary Layer Theory*, 8th ed., Springer, New York.
- Shaw, D. A., and T. J. Hanratty (1977), Turbulent mass transfer rates to a wall for large Schmidt numbers, *AIChE J.*, *23*(1), 28–37.
- Stacey, M. T., S. G. Monismith, and J. R. Burau (1999), Measurements of Reynolds stress profiles in unstratified tidal flow, *J. Geophys. Res.*, *104*, 933–910,949.
- Steinberger, N., and M. Hondzo (1999), Diffusional mass transfer at sediment-water interface, *J. Environ. Eng.*, *125*, 192–199.
- Sveen, J. K. (2004), An introduction to MatPIV v. 1.6.1, in *Mechanics and Applied Mathematics*, Dept. of Mathematics, University of Oslo.
- Tanaka, T., and J. K. Eaton (2007), A correction method for measuring turbulence kinetic energy dissipation rate by PIV, *Exp. Fluids*, *42*, 893–902.
- Townsend, A. A. (1976), *The Structure of Turbulent Shear Flow*, 2nd ed., 429 pp., Cambridge Univ. Press, Cambridge.
- Zhu, W., R. van Hout, L. Luznik, H. S. Kang, J. Katz, and C. Meneveau (2006), A comparison of PIV measurements of canopy turbulence performed in the field and in a wind tunnel model, *Exp. Fluids*, *41*, 309–318.
-
- M. Hondzo, St. Anthony Falls Laboratory, Department of Civil Engineering, Mississippi River at Third Ave. SE, University of Minnesota, Minneapolis, MN 55414, USA.
- M. Limm, Department of Integrative Biology, 3060 Valley Life Sciences Bldg., University of California, Berkeley, CA 94720, USA.
- M. A. Reidenbach, Department of Environmental Sciences, University of Virginia, 291 McCormick Rd., PO Box 400123, Charlottesville, VA 22904, USA. (reidenbach@virginia.edu)
- M. T. Stacey, Department of Civil and Environmental Engineering, 665 Davis Hall, MC 1710, University of California, Berkeley, CA 94720, USA.